

PARAMETRIC STUDIES OF FLEXIBLE SANDWICH PANELS AS A COMPLIANT FAIRING FOR FOLDING WINGTIP JOINTS

Nuhaadh Mohamed Mahid*, Mark Schenk, Branislav Titurus, Benjamin King Sutton Woods

University of Bristol, Bristol, United Kingdom

ABSTRACT

This paper presents a parametric study into the design space of morphing fairings for the Semi-Aeroelastic Hinged (SAH) folding wing concept. The fairing will cover the angled hinge region of the wingtip with a smooth and continuous skin surface to reduce drag. It is made from flexible sandwich panels employing the Geometrically Anisotropic ThermOplastic Rubber (GATOR) morphing skin concept, with a chevron-based cellular core covered in elastomeric facesheets. A parametrically defined finite element analysis framework is established and used to explore the mechanical response of a three-dimensional wing fairing. The two design objectives are minimising torsional stiffness and out-of-plane deformation during the rotation of the underlying wingtip joint. A parameter sweep is used to establish correlations between the design variables and the competing objectives. Notable correlations were identified for the chevron wall angle, core thickness, facesheet thickness, fairing span, pre-strain and flare angle. Pre-straining the facesheets is found to delay the onset of large changes in surface curvature and the subsequent softening of stiffness. However, it also leads to higher levels of torque at large rotation angles. Overall, this study helps to elucidate the design trends for compliant fairings while also reducing the design space in preparation for further studies.

Keywords: Morphing Structures, Folding Wingtip, Sandwich Panel

NOMENCLATURE

Abbreviations

WRBM Wing Root Bending Moment

SAH Semi-Aeroelastic Hinge

GATOR Geometrically Anisotropic ThermOplastic Rubber

PPMCC Pearson Product Moment Correlation Coefficient

Wing Section Variables

Λ Flare angle [deg]

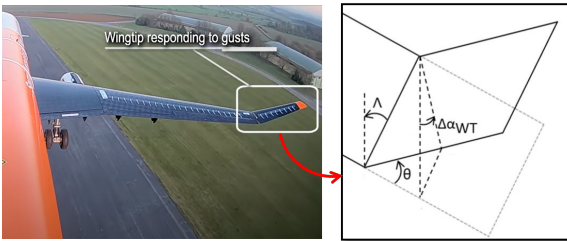
θ Folding angle [deg]

ϕ_m	Material offset angle [deg]
L	Span [m]
c	Chord [m]
ε_p	Pre-strain across the hinge
<i>Panel Variables</i>	
θ_c	Chevron angle [deg]
l_c	Chevron wall length [mm]
t_c	Chevron thickness [mm]
d	Chevron separation [mm]
t_r	Rib thickness [mm]
B	Core thickness [mm]
t_f	Facesheet thickness [mm]

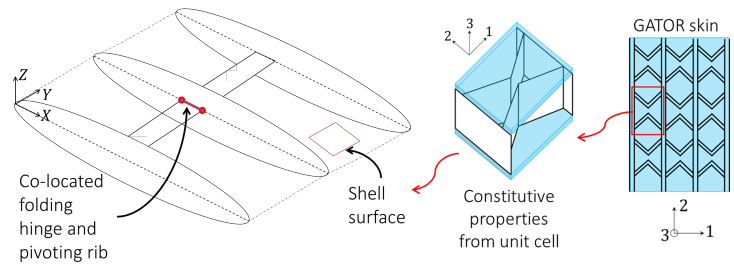
1. INTRODUCTION

Engineers spend a lot of effort designing more aerodynamically and structurally efficient wings in the drive for reduced environmental impact and operating costs. A particularly important design variable is wing span, as longer wings with higher aspect ratios have lower induced drag. Reduced induced drag in commercial aircraft reduces fuel consumption, hence the operating cost of the airlines. The primary constraint against having longer wings is the limited airport gate size and the impact it has on the wing structural design due to increased wing root bending moments (WRBM). These constraints are effectively circumvented by the Semi-Aeroelastic Hinge (SAH) wingtip concept [3] shown in Figure 1a. It consists of a hinged wingtip extension that can be actively and passively rotated on the ground (to reduce span for gate clearance) and during flight (to alleviate gust loads). Releasing the wingtip to fold up freely with the gust reduces the lift generated and removes the bending moment about the hinge axis. The lift reduction effect is further compounded by the outward skew of the hinge axis to a flare angle Λ from the line of flight. This creates a geometrical coupling between the wingtip rotation and the local pitch of the wingtip, which reduces the wingtip pitch as it rotates, thereby further reducing lift generation. Aeroelastic studies on the SAH concept have shown gust load alleviation characteristics [2, 3] which reduces the peak WRBM. This enables increasing the wingspan with reduced requirement for further re-

*Corresponding author: nuhaadh.mahid@bristol.ac.uk



(a) Semi-Aeroelastic Hinge concept [1, 2].



(b) Pivoting-rib fairing concept with GATOR skin.

FIGURE 1: COMPLIANT FAIRING FOR FOLDING WINGTIP JOINT.

inforcement of the wing structure (e.g., only a 4.4% increase in peak WRBM despite a 25% increase in wingspan [2]).

While the SAH concept provides significant wing/aircraft level benefits, including a hinge in the wing creates a local aerodynamic issue. The joint includes a hinge mechanism and an actuation and clutching system mounted coaxially to the hinge line. These components increase the wing's thickness locally, and due to the flare angle, this thickened region of the wing is not aligned with the airflow. Furthermore, the SAH wingtip is envisioned to need a rotation range of roughly -20 (downwards) to +90 degrees (upwards) around the hinge axis [4]. Achieving this large range of motion complicates the design of a mechanism-based fairing solution to enclose the joint and actuation components.

To reduce the aerodynamic penalty of the SAH concept at the local hinge region, this work will explore the use of compliance-based morphing sandwich structures to create a continuous, smoothly deforming fairing over the joint region. It will build on the concept of a SAH joint fairing originally proposed by the authors [5], which combines a rotating rib positioned around the joint with compliant sandwich skin panels. The joint architecture is illustrated in Figure 1b. It shows a central rib pivoted to the folding joint, forming a hinged connection between the inboard wing and the wingtip. The pivoting rib enables the deformation of the fairing to be distributed over a longer spanwise length, thereby reducing the overall strain on the fairing and the torsional stiffness of the joint [5]. The fairing which covers the joint is a sandwich panel with a cellular core and elastomer facesheets. The panel design is based on the concept of Geometrically Anisotropic ThermOplastic Rubber (GATOR) skin [6, 7], which enables 3D printing of the core and factsheets together with thermoplastic materials. The type of core used in the sandwich panel strongly affects the equivalent elastic properties of the panel. Hence, the equivalent properties of various types of cellular cores have been studied for numerous applications [8, 9].

This paper explores the design space achievable with GATOR morphing sandwich panels as a fairing for folding wingtip joints. The novelty of the study is in the framework developed to model and analyse the effects of the fairing over the 3D geometry of the wing. It also presents correlations and trade-offs not identified in the previous analytical study that introduced this fairing concept [5]. The following sections first discuss the modelling approach taken to homogenise the stiffness properties of the morphing panel into equivalent shells in order to reduce the computational cost, followed by details of how the finite element simulations using these equivalent shells were parameterised and

run. The design space was then explored through a large number of FE runs using Latin Hypercube sampling across the upper and lower bounds of each design variable. The study sought to find designs which provide a high degree of flexibility in folding deformation along with minimal distortion to the cross-section shape of the wing. Correlation analysis was carried out to identify the variables which dominate the response. Finally, simple parameter sweeps are used to explore more explicitly the effects of varying individual design parameters about a given baseline design.

2. MODELLING

This section presents the analysis framework used to seek the designs which reduce overall torsional stiffness and warping of the skin panels. The design variables used are of two categories — the sandwich panel variables and the morphing wing section variables. The analysis process is performed separately on each category of design variables to identify the independent effects of each component on the objectives. It is, however, important to explore the interactive effects of different combinations of panel and wing section variables to get a complete representation of the fairing behaviour. Hence, this should be explored in future work.

The analysis process is made up of two steps. Firstly, the homogenised mechanical properties of the sandwich panel are evaluated using an analytical approach. This gives an equivalent shell stiffness matrix for the panel. Secondly, the folding of the wing section is modelled in a finite element analysis framework using equivalent thin-walled shell properties. The analytical shell stiffness matrix from the first step provides the constitutive model for the second step. This two-step approach simplifies the analysis and significantly reduces the computational cost.

The analysis process for each category of design variables is performed twice. In the first study, Latin Hypercube Sampling is used to identify the correlations between the selected design variables and the objectives. In the second study, the correlated design variables are varied parametrically to evaluate the effect of each variable on the objectives.

2.1 Constitutive model of the GATOR morphing panels

The morphing skin panel has a cellular core and elastomeric facesheets that are assumed to be made of homogeneous and isotropic materials. The materials are selected to match previous work on the GATOR concept [7], with both the core and facesheets being made from 3D-printed Thermoplastic Polyurethane (TPU). A softer TPU formulation (Ninjaflex, manufactured by NinjaTek, with a Shore Hardness = 85A) is used

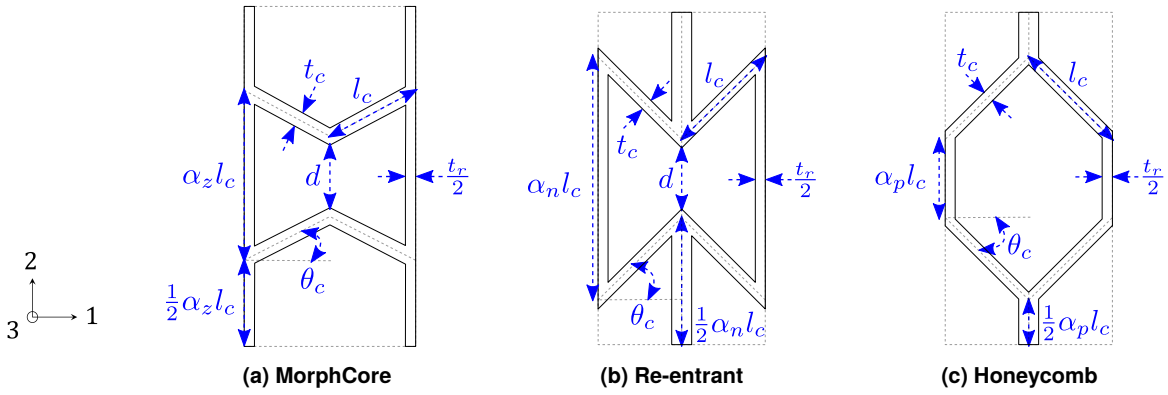


FIGURE 2: UNIT CELL GEOMETRY OF THE CELLULAR CORES. (A) MORPHCORE [10], (B) RE-ENTRANT AND (C) HONEYCOMB CELLULAR CORES HAVE ZERO, NEGATIVE AND POSITIVE POISSONS RATIOS, RESPECTIVELY.

for the facesheets and a harder formulation (Armadillo, also from NinjaTek, Shore Hardness = 75D) for the core. The material behaviour is assumed to be linear elastic with the properties shown in Table 1.

TABLE 1: ELASTIC PROPERTIES OF THE PANEL MATERIALS [7]

Material	Youngs Modulus [MPa]	Poissons Ratio
Ninjaflex	12	0.48
Armadillo	396	0.48

Three different unit cell geometry configurations were explored for the cellular core, as shown in Figure 2. The variations in the connectivity and orientation of the bending members in these cores create zero (ZPR), negative (NPR) and positive (PPR) Poisson's ratios. Each unit cell comprises hexagonal (regular or irregular) shapes with either different chevron wall angle θ_c or tessellation patterns. For instance, a re-entrant core is a variation of honeycomb core where the chevron wall angle θ_c is measured in the opposite direction. Moreover, the MorphCore is made up of hexagonal shapes which are aligned to form continuous vertical “ribs” within the core.

For clarity, the dimensions of the unit cell are referred to as length, width and height in 1-, 2-, and 3-axis directions, respectively. Note that the unit cell would have a different width for each core type with the same set of input variables. The width of the unit cell would affect the derived equivalent properties. Hence, for a fair comparison of the core types, these widths are made uniform by adjusting the length of the 2-axis wall of the hexagonal shape by a factor α_i where $i \in [z, n, p]$. These scaling factors are evaluated as

$$\alpha_z = \alpha, \quad \alpha_n = \alpha + \sin \theta_c, \quad \alpha_p = \alpha - \sin \theta_c \quad (1)$$

where α is a parameter that is set to enforce a minimum separation between the chevron tips. The minimum value of α required to ensure non-overlapping chevrons in ZPR and NPR cores is given by

$$\alpha \geq 2 \sin \theta_c + \frac{t_c}{l_c} \sec \theta_c \quad (2)$$

Due to its geometrical shape, the PPR core will always have a chevron tip separation greater than that of ZPR and NPR cores.

Hence, the chevron tip separation d is not defined for the PPR core. Instead, the α value evaluated for ZPR and NPR cores is used to evaluate the scaling factor for the PPR core. Hence, α is set to be the same for all cell types and is evaluated as

$$\alpha = \alpha_{min} + \frac{d}{l_c} \quad (3)$$

where α_{min} is the limit value in Equation 2.

The three types of cores described have been extensively studied in the literature. A detailed study of the hexagonal shape in honeycomb and re-entrant cores are presented by Olympio *et al* [11], and a study of the MorphCore panels for 1D morphing application is presented by Bubert *et al* [8]. The equivalent stiffness properties of the cores are evaluated using an adapted set of analytical expressions from Olympio *et al* [9]. This is shown in Table 2 where the factor $\kappa = 2.4 + 1.5\nu$. E and ν are Young's modulus and Poisson's ratio of the core material. β and η are the thickness-to-length ratio normalised thicknesses of the chevrons and the thickness ratio of ribs-to-chevrons evaluated as $\beta = t_c/l_c$ and $\eta = t_r/t_c = t_r/l_c$, respectively. These expressions account for the bending, shear and axial deformation of the walls of the hexagonal shape. In these expressions, the factor γ_i where $i \in [n, p]$ is used to alter the direction of the chevron angle measurement for honeycomb ($\gamma_p = 1$) and re-entrant ($\gamma_n = -1$) cores.

The equivalent shell stiffness matrix of the panel is evaluated using the classical laminate theory. This approach is an extension of the classical plate theory applied to laminated composite panels of orthotropic and homogeneous layers. Hence, it uses the kinematic assumption of the thickness of the plate remaining unchanged and straight lines normal to the mid-plane remaining straight and perpendicular to the mid-plane after deformation. This approach ignores the effects of transverse shear strains through the thickness of the panel. The model accuracy for the relatively thick sandwich panels studied here may ultimately benefit from the inclusion of transverse shear deformations, but for this initial study, they are ignored.

The finite element analysis for the wing section is carried out in Abaqus. The finite-strain shell element (S4R) used for the analysis is based on first-order shear deformation theory [12], which assumes that the straight lines normal to the midplane remain straight but not necessarily normal to the midplane after

TABLE 2: ANALYTICAL EXPRESSIONS ADAPTED FROM OLYMPIO AND GANDHI [9] FOR EQUIVALENT STIFFNESS OF THE CORES

	Honeycomb / Re-entrant core	MorphCore
$\frac{E_x}{E}$	$\frac{\beta^3 \cos(\gamma_i \theta_c)}{\sin^2(\gamma_i \theta_c)(\alpha_i + \sin(\gamma_i \theta_c))(1 + \beta^2(\kappa + \cot^2(\gamma_i \theta_c)))}$	$\frac{\beta^3}{\alpha_i \cos(\theta_c)(\beta^2 + \tan^2(\theta_c)(1 + \kappa\beta^2))}$
$\frac{E_y}{E}$	$\frac{\beta^3(\alpha_i + \sin(\gamma_i \theta_c))}{\cos^3(\gamma_i \theta_c)(1 + \beta^2(\kappa + \tan^2(\gamma_i \theta_c)) + 2\frac{\alpha_i}{\eta} \sec^2(\gamma_i \theta_c))}$	$\frac{\eta\beta}{2 \cos(\theta_c)}$
ν_{xy}	$\frac{\cos^2(\gamma_i \theta_c)(1 + \beta^2(\kappa - 1))}{\sin(\gamma_i \theta_c)(\alpha_i + \sin(\gamma_i \theta_c))(1 + \beta^2(\kappa + \cot^2(\gamma_i \theta_c)))}$	0
$\frac{G_{xy}}{E}$	$\frac{\beta^3(\alpha_i + \sin(\gamma_i \theta_c))}{F\alpha_i^2 \cos^2(\gamma_i \theta_c)}$	$\frac{\beta^3 \cos(\theta_c)}{H}$
$F = 1 + 2\frac{\alpha_i}{\eta^3} + \frac{\beta^2}{\alpha_i^2} \left(\alpha_i \kappa \left(\frac{2}{\eta} + (\alpha_i + \sin(\gamma_i \theta_c)) \right) + (\alpha_i + \sin(\gamma_i \theta_c)) (\sin(\gamma_i \theta_c) + \tan^2(\gamma_i \theta_c)(\alpha_i + \sin(\gamma_i \theta_c))) \right)$		
$H = 2\frac{\alpha_i^2}{\eta^3} \cos^2(\theta_c) \left(1 + \kappa \left(\frac{\beta \eta}{\alpha_i} \right)^2 \right) + \alpha_i (4 \cos^2(\theta_c)(1 + \kappa\beta^2) + \beta^2 \sin^2(\theta_c))$		

deformation. This formulation approximates the shear stresses, which are parabolic across the thickness of the plate for static bending [13], as a uniform value across the thickness. Hence, it requires shear correction factors to evaluate the transverse shear stiffness matrix using the transverse shear moduli (i.e., G_{13} and G_{23}). A closed-form analytical expression for shear correction factors is not available for the general case [14]. In this study, for simplicity, the transverse shear stiffness matrix was not explicitly defined. Instead, it was approximated by Abaqus [15] using the in-plane components of the shell stiffness matrix as

$$K_{11} = K_{22} = \frac{1}{6}(A_{11} + A_{22}) + \frac{1}{3}A_{66}, \quad K_{12} = 0 \quad (4)$$

where K_{11} and K_{22} are the transverse shear stiffness in the 13-plane and 23-plane of the panel, and K_{12} is the coupling term between the two shear planes.

2.2 Shell model of the wing section

The parametric study pursued here requires the repetitive generation of finite element models for various geometries of the wing section and panel thicknesses. Hence, a parametrically defined model geometry generator was written and coupled to an input/output wrapper script around Abaqus to automate the process within an analysis framework. This section describes the framework for the wing section model. Note that a half model was used for the symmetric cases (where there were no taper, sweep or flare angle).

The geometry definition was done in three steps. Firstly, the ribs' coordinate locations in the wing's midplane (i.e., X and Y coordinates) were defined. Secondly, the aerofoil thickness equation and local chord length (for scaling) were used to define the outer wing section (i.e., Z coordinate for the rib profile nodes). Finally, the rib profile nodes were offset inward by half the thickness of the skin panel to define the skin's midplane surface. These

steps are described in detail as follows.

The ribs' midplane coordinates accounting for sweep and taper are defined by Equation 5. It describes a line (for variables X and Y) along the span at a given normalised chord x of the wing. Parameters c and L are the root chord and the span, as shown in Figure 3b. Parameters ϕ and T are sweep angle and taper ratio, which in this case are 0 and 1, respectively. Another line along the chord of a rib rotated by flare angle Λ about a pivot point is given by Equation 6. The pivot point (X_Λ, Y_Λ) is the reference location of each rib. These reference locations are referred to as beam nodes and are highlighted as red crosses in Figure 3a and 3b. Note that in this study, the reference location for the rib is defined at a constant normalised chord x_Λ of 0.5. Hence, Y_Λ is the only independent parameter as X_Λ is evaluated from Equation 5 for any given normalised chord location x_Λ . The Equations 5 and 6 are combined to give the Equation 7, which for any distribution of normalised chord locations $x \in [0, 1]$ and spanwise rib locations $Y_\Lambda \in [0, L]$, gives the Y coordinates of the wing's midplane grid points. These Y coordinates are then used in Equation 5 to evaluate the X coordinate of the midplane grid points. Note that the flare angle Λ is set to be the same for all ribs in this study; however, they need not be the same, and the effects of non-uniform Λ across the ribs shall be explored in future work.

$$X = Y \sin \phi + xc \left(1 - \frac{Y}{L}(1 - T) \right) \quad (5)$$

$$X = X_\Lambda - (Y - Y_\Lambda) \cot \Lambda \quad (6)$$

$$Y = \frac{c \left(x_\Lambda \left(1 - \frac{Y_\Lambda}{L}(1 - T) \right) - x \right) + Y_\Lambda (\cot \Lambda + \sin \Lambda)}{\cot \Lambda + \sin \Lambda - xc \frac{1}{L}(1 - T)} \quad (7)$$

The rib profile (i.e., Z coordinate) is defined in the sec-

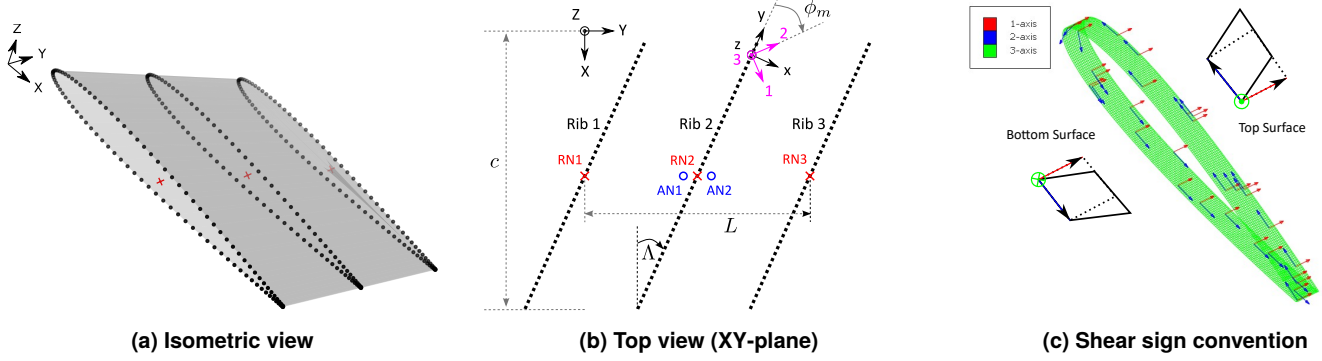


FIGURE 3: NODES, COORDINATE SYSTEMS AND SIGN CONVENTIONS OF THE MODEL. NOTE THAT NODES AN1 AND AN2 ARE CO-LOCATED WITH RN2 (SHOWN SEPARATED FOR CLARITY). RIB PROFILE NODES ARE SHOWN IN BLACK AND BEAM NODES ARE IN RED.

ond step for the wing's midplane points using the equation for NACA 0015 profile. The choice of a symmetric aerofoil is solely based on keeping the analysis simple by avoiding non-zero folding angles due to applied pre-tensioning of the skin. Note that the aerofoil equation defines the outer surface of the wing's cross-section. For FE analysis, however, the shell surface defining the midplane of the skin panels is required. Hence, the rib profile nodes R are offset inward by half the thickness of the panel by the expression

$$P_{ij} = R_{ij} + \frac{T_p}{2} \hat{n}_{ij} \quad \text{where} \quad R_{ij} = [X \quad Y \quad Z]^T \quad (8)$$

P_{ij} is the skin panel's midplane nodes and the subscript i, j corresponds to the local indices of the grid. \hat{n}_{ij} is the inward pointing unit normal vector and T_p is the thickness of the panel. Note that the top and bottom surfaces of the panel's midplane profile may cross over towards the trailing edge after the offset. This cross-over point, which could be determined by interpolation, is the new trailing edge for the panel's midplane profile. An example of the rib nodes generated using this approach is shown in Figure 3a.

The geometry and the mesh for the fairing are created using GMSH [16]. A structured quadratic element mesh is created for the shell surface and saved as an “*.inp” file. The mesh comprises of “S4R” finite-strain shell elements of a maximum length of 10 millimetres, with 6 degrees of freedom at each node. The constitutive properties, material orientation, constraints and loading steps information are added to the end of the file for FE analysis in Abaqus. The constitutive properties of the shell elements are defined using the equivalent shell stiffness matrix calculated using the approach described in the previous subsection. The material orientation is defined by the 123-axes shown in Figure 3b. The 123-axes is defined at a clockwise angle ϕ_m (referred to as material offset angle) to the hinge axis, which is shown as the xyz-axes in the figure.

The model is constrained using two additional anchor nodes, AN1 and AN2, which are co-located with the beam node RN2. This is shown in Figure 3b, where beam nodes are marked in red and anchor nodes in blue. AN1 is fixed in all degrees of freedom, and AN2 is connected to AN1 via a “JOIN, REVOLUTE” connector. The “JOIN” constraint restricts the translation degrees of freedom of AN2 to be the same as that of AN1. The “REVOLUTE” constraint restricts the rotational degrees of freedom of AN2 to a single pre-defined axis, which in this case is the hinge

axis (i.e., y-axis in Figure 3b). The nodes of Rib 1 are rigidly connected to the anchor node AN1 via a “TIE” constraint. A “TIE” constraint results in a rigid body where the forces on the slave nodes are passed onto the master node, and the deformation on the master node translate to the slave nodes. Additional constraints are defined based on whether the model is a full-model or a half-model, as summarised in Table 3. Note that a half-model does not have rib 3. The loading rotation is applied to AN1 to fold the wingtip. Half of the defined rotation value for the full-model is used for the half-model.

TABLE 3: ADDITIONAL CONSTRAINTS DEFINED WHICH ARE DIFFERENT FOR FULL AND HALF MODEL

Full-model

- Rib 2 nodes are connected to RN2 via a “TIE” constraint
- Rib 3 nodes are connected to AN2 via a “TIE” constraint
- RN2 node is connected to AN1 via a “JOIN, REVOLUTE” connector

Half-model

- Rib 2 nodes are connected to AN2 via a “TIE” constraint

The model is loaded in two steps. In the first step, a pre-tension is applied to the panels across the hinge using a unit temperature change and artificial coefficient of thermal expansion. This is achieved by defining a thermal load vector \mathbf{F} . Note that the shell section response is defined as

$$\mathbf{N} = \begin{bmatrix} \mathbf{A} & \mathbf{B} \\ \mathbf{B} & \mathbf{D} \end{bmatrix} \boldsymbol{\varepsilon} - \mathbf{N}_{thermal} \quad \text{where} \quad \mathbf{N}_{thermal} = \Delta T \mathbf{F} \quad (9)$$

\mathbf{N} is the forces and moments vector, $\boldsymbol{\varepsilon}$ is the strains and curvatures vector, \mathbf{F} is the vector of forces and moments caused on a fully constrained shell due to unit temperature change, and ΔT is the applied temperature change. In this case, temperature change ΔT is set to be -1. Hence, the pre-strain is varied by changing the thermal load vector \mathbf{F} . Note that \mathbf{F} is defined in the material axes and the pre-strain across the hinge is defined in the hinge axes. Hence, \mathbf{F} is evaluated using the shell stiffness matrix and the transformed strains as

$$\mathbf{F} = \begin{bmatrix} \mathbf{A} & \mathbf{B} \\ \mathbf{B} & \mathbf{D} \end{bmatrix} \boldsymbol{\varepsilon}_{123} \quad \text{where} \quad \boldsymbol{\varepsilon}_{123} = \mathbf{R} \mathbf{T} \mathbf{R}^{-1} \boldsymbol{\varepsilon}_{xyz} \quad (10)$$

\mathbf{R} is the Reuter's matrix and \mathbf{T} is the transformation matrix which defines the rotation from hinge axes to material axes. The pre-strain is defined only in the in-plane direction across the hinge, and the skin panel is symmetric, resulting in a null \mathbf{B} matrix. Hence, the thermal load vector \mathbf{F} simplifies to having non-zero values only for the force terms.

The material axes for each element are defined by projecting a cylindrical coordinate system to the shell surfaces: meaning that the 2-axis of the elements is in the opposite direction on the top and bottom surfaces of the wing, as illustrated in Figure 3c. This results in a shear sign convention which is in the opposite direction for the surfaces when observed from the global reference. Hence, applying the same thermal load vector \mathbf{F} on the top and bottom surfaces would result in a non-zero folding angle on the hinge. To resolve this, the shell section properties were defined independently for the top and bottom surfaces. Note that the shell normal is pointing outward, which thereby requires the rotation angle to transform the pre-strain from the hinge axis to the local material axis to be in the opposite direction for the top and bottom surfaces. For a symmetric wing profile, the resulting thermal load vector \mathbf{F} for the top and bottom surfaces are identical except for the opposite sign of the shear (and torsion) term.

The second loading step is the rotation applied to the AN2 node to fold the wingtip. Note that in Abaqus, rotations are applied in the global coordinate system, whereas the folding of the wingtip is about the y-axis (but in opposite direction) in the hinge coordinate system. Hence, the component of the folding angle in the global X-axis is defined as

$$\theta_X = \theta \cos \Lambda \quad (11)$$

where θ is positive for wingtip folding up. As the rotation of the AN2 node is restricted to the hinge axis (i.e., y-axis), for the node to rotate about X-axis it must also rotate about Y-axis (for non-zero Λ). Hence, applying only θ_X rotation about X-axis will achieve θ rotation about the hinge axis. Note that half the θ_X rotation is applied for the half-model due to the symmetric boundary conditions used. Moreover, in the post-processing stage, the rotation and the resultant torque around the hinge axis due to loading steps are evaluated as

$$\theta = \frac{\theta_X}{\cos \Lambda}, \quad M = \frac{M_X}{\cos \Lambda} \quad (12)$$

using the rotation and moment values in the Abaqus output. These results are automatically extracted from the “*.odb” file using a Python script for further post-processing and visualisation.

The folding stiffness of the fairing is visualised as an equilibrium plot of applied rotation against the reaction torque about the hinge. Given the complexity of the three-dimensional shapes explored and their deformation response when folding, a globally integrated curvature metric was used to keep track of the amount of shape change on the fairing. Specifically, the volume-averaged root mean square of curvatures of the shell elements is used as the curvature metric, as expressed by

$$C = \sqrt{\frac{\sum V_i \kappa_i^T \kappa_i}{\sum V_i}} \quad \text{where} \quad \kappa_i = [\kappa_{11}, \kappa_{22}, \kappa_{12}]^T \quad (13)$$

κ_i and V_i are each element's curvatures and volume, respectively. This approach is more robust than simply tracking deformations for particular discrete points and is more globally representative than tracking changes in projected 2D aerofoil shapes.

3. RESULTS AND DISCUSSION

The analysis was carried out in three stages. The aim of the first and second stages is to identify the correlations between the various design variables and the objectives. The third stage aims to parametrically study the influence of the more highly correlated variables on the objectives. In all three stages the inboard chord c is set to 1.64 metres at the reference location of the first rib (i.e., at RN1), as shown in Figure 3b. The beam nodes are located at 50% chord. The baseline configuration wing section is symmetric and has no sweep or taper. The wing section is deformed with an applied folding angle of 80 degrees for the full-model (and a rib rotation angle of 40 degrees for the half-model). The finite element simulation is initially run with Newton's solver. The cases which fail to converge are re-run with the dynamic implicit solver to find the quasi-static solution.

3.1 Panel geometry study

For the panel study, the wing section parameters are fixed to the baseline configuration values shown in Table 4. The flare angle and the material offset angles are zero, making the model symmetric. Hence, the half-model was used to reduce the computational cost. The study was performed on a set of 300 points generated by Latin Hypercube sampling for the variables and ranges shown in Table 5. These sampled points were used to analyse all three types of cores: namely, ZPR, NPR and PPR cores. Hence, a total of 900 cases were analysed, from which 879 converged (and 21 failed) results were obtained.

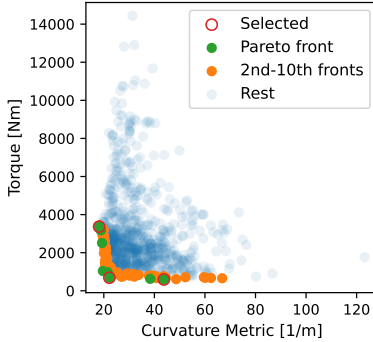
TABLE 4: FIXED PARAMETERS FOR THE PANEL STUDY

Parameter		Value	Unit
Pre-strain across the hinge	ε_p	0	
Span	L	0.82	m
Hinge flare angle	Λ	0	deg
Material offset angle	ϕ_m	0	deg

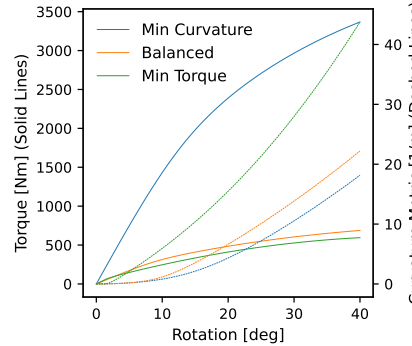
TABLE 5: VARIABLE RANGES FOR THE PANEL STUDY

Variable		Minimum	Maximum	Unit
Chevron angle	θ_c	10	80	deg
Chevron wall length	l_c	5	20	mm
Chevron thickness	t_c	1	3	mm
Chevron separation	d	5	20	mm
Rib thickness	t_r	1	3	mm
Core thickness	B	5	30	mm
Facesheet thickness	t_f	1	5	mm

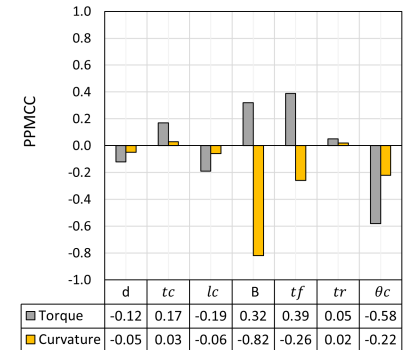
The distribution of the solutions against the two objectives is shown in Figure 4a. In order to identify the most promising configurations, a non-dominated sorting algorithm was used to extract the Pareto optimal solutions along the Pareto frontier. As these results are not from a formal optimisation procedure,



(a) Hierarchical Pareto fronts



(b) Torque-Curvature plot



(c) PPMCC for panel variables

FIGURE 4: TORQUE, CURVATURE AND PPMCC FROM THE PANEL VARIABLES STUDY.

there were, not surprisingly, only a few points on the frontier. Therefore, the pool of good solutions was expanded beyond those that were strictly Pareto optimal through an iterative process of non-dominated sorting, where the previously determined Pareto optimal points were removed from the dataset before re-running the non-dominated sorting algorithm to find the next best set of points. This process was repeated such that the top 10 “frontiers” of the solutions space were combined into a set of 84 points, as highlighted in the figure. The three best solutions from the Pareto front are selected, and their performance with respect to the objective functions is shown in Figure 4b. It shows the torque and curvature response against the folding angle for the solution with minimum curvature, minimum torque and a balanced value of the two objectives. Note that the balanced solution achieves an 80% reduction in torque at the cost of a 22% increase in curvature metric relative to the minimum curvature solution. Conversely, it achieves a 49% reduction in the curvature metric at the cost of a 16% increase in torque relative to the minimum torque solution. This illustrates the competitive trade-off between the objectives for the solutions on the Pareto front.

In order to elucidate underlying design trends, the relationship between the objectives and the design variables is quantified using the Pearson Product Moment Correlation Coefficient (PPMCC), which is calculated for each variable against each objective. PPMCC is a non-dimensional value which could range from -1 to 1. A value of 0 indicates no correlation, a value of -1 indicates a perfectly negative correlation, and a 1 indicates a perfectly positive correlation.

The PPMCC evaluated for the converged solutions are shown in Figure 4c. It shows a stronger negative correlation between core thickness and curvature compared to the strength of the positive correlation between core thickness and torque. Conversely, it also shows a stronger positive correlation between facesheet thickness and torque compared to the strength of the negative correlation between facesheet thickness and curvature. Hence, it indicates that a likely balanced solution will have a thick core with thin facesheets. Moreover, the figure shows a notable correlation between the chevron angle and the objectives. Note that this dataset includes the cores of three different types. Hence, the effect of the chevron angle on the objectives is explored separately for each core type in the following carpet plots.

A PPMCC cannot be calculated for core type. Hence, the

percentage of each core type in the top 10 fronts, shown in Table 6, is used to indicate the efficacy of each core type. ZPR core forms the majority of these solutions, indicating its advantage over the NPR and PPR cores for morphing fairing applications. This is in agreement with the conclusions drawn by Olympio *et al* [9] in the analytical study of these core types for 1-D morphing applications.

TABLE 6: NUMBER OF EACH CORE TYPE IN THE TOP 10 HIERARCHY OF SOLUTIONS

NPR cores	PPR cores	ZPR cores
24 (28.6%)	15 (17.9%)	45 (53.6%)

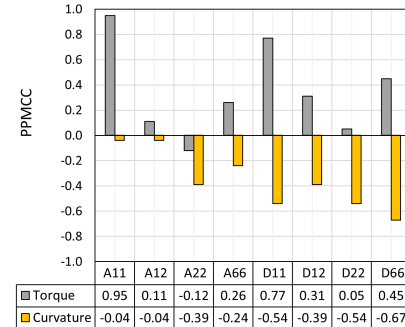


FIGURE 5: PPMCC FOR SHELL STIFFNESS MATRIX

The correlations between the components of the shell stiffness matrix and the objectives are shown in Figure 5. It shows a strong correlation with torque for A_{11} and D_{11} , indicating the significance of flexibility in the direction across the hinge in reducing torque. Additionally, a notable correlation is identified between torque and D_{66} , which indicates the significance of torsional deformation κ_{12} of the panel as the wingtip folds. The curvature metric shows a notable correlation with components of the out-of-plane stiffness matrix (i.e., “D” matrix). Note that the PPMCCs for the components of the shell stiffness matrix are generally stronger than that of the panel variables. This could be due to the interdependence between the components of the shell stiffness matrix. For instance, the thickness of the core and facesheets, which shows a strong correlation with the objectives, contributes to all the components of the shell stiffness matrix.

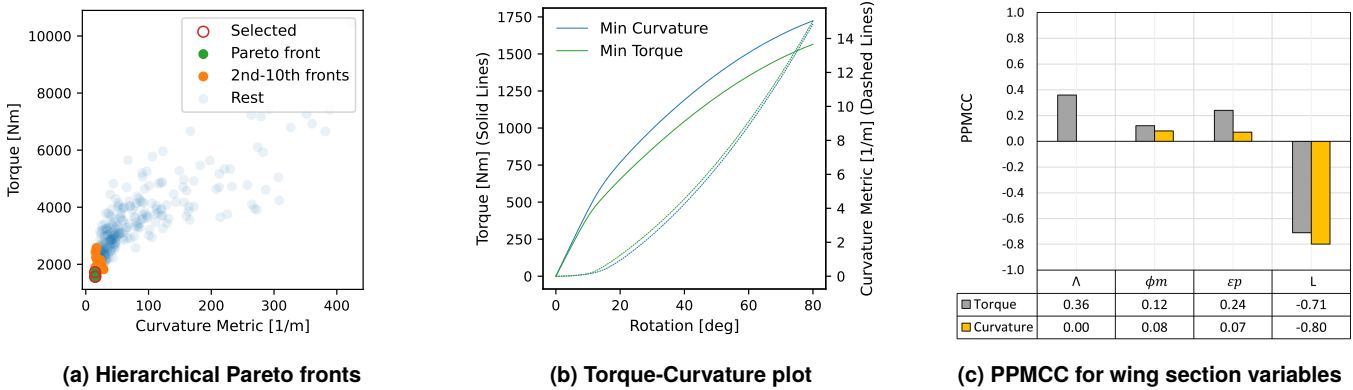


FIGURE 6: TORQUE, CURVATURE AND PPMCC FROM THE WING SECTION VARIABLES STUDY.

3.2 Fairing geometry study

The correlations between the wing section variables and the objectives were identified using the fixed set of panel variables shown in Table 7. The design space of the fairing variables was analysed using 300 points generated by Latin Hypercube sampling for the variables and their ranges shown in Table 8. This resulted in 267 converged solutions, which were classified into hierarchical fronts shown in Figure 6a. The small range of values for both the objectives in the top 10 fronts indicates that the objectives space is less competitive for the set of parameters being varied. This is further highlighted by the similar torque and curvature plot for both minimum curvature and minimum torque solution shown in Figure 6b. The final torque values show a difference of $\pm 5\%$, whereas the difference for the curvature metric is $\pm 1\%$.

TABLE 7: FIXED PARAMETERS FOR THE FAIRING STUDY

Parameter		Value	Unit
Chevron angle	θ_c	45	deg
Chevron wall length	l_c	12.5	mm
Chevron thickness	t_c	2	mm
Chevron separation	d	12.5	mm
Rib thickness	t_r	2	mm
Core thickness	B	17.5	mm
Facesheet thickness	t_f	3	mm

TABLE 8: VARIABLE RANGES FOR THE FAIRING STUDY

Variable		Minimum	Maximum	Unit
Flare angle	Λ	0	30	deg
Material offset angle	ϕ_m	-40	40	deg
Span	L	0.246	1.23	m
Pre-strain	ε_p	0	0.25	

The PPMCC for the wing section variables are shown in Figure 6c. It shows the strongest correlation between span and curvature, indicating that a long span would reduce the curvature metric. It also shows a strong negative correlation between span and torque. A notable positive correlation is shown for torque with flare angle and applied pre-strain. Note that for each variable, the correlations it has with the objectives are in the same direction.

This results in the less competitive objective space shown in the 6a. The design variables which are highly correlated with the objectives are studied further in the following carpet plots.

3.3 Parametric study of correlated variables

The parametric study uses the values shown in Table 4 and Table 7 for the fixed parameters of the wing section and the panel, respectively. Two variables are parametrically varied in each study, and the resulting values of the objectives are plotted in a carpet plot. All of the parametric studies shown in Figure 7 and 8 use the half-model except for the non-symmetric case in Figure 8b where the full model was used.

The effect of applied pre-strain and the chevron angle on different types of cores are shown in Figure 7. The ranges of both axes are held constant for all core types for direct visual comparison between the responses of the cores. The ZPR core shows the smallest ranges of values for both objectives. The largest range of values for torque is in the NPR core, and the largest range of values for curvature is in the PPR core. The figure also shows that for all core types, the changes in values of both objectives are greater for a step change in chevron angle from 45 to 62.5 degrees compared to the same step change from 62.5 to 80 degrees. This is attributed to the increasing gain in axial (i.e., 1-axis in Figure 2) stiffness with smaller chevron angles. At high chevron angles, the axial deformation of the core mainly comes from the bending of the chevron. At small chevron angles, the bending contribution of the chevron is reduced, resulting in a much higher overall stiffness due to the lengthwise stiffness of the chevron walls. While this behaviour is seen for all core types, note that the PPR core with an 80-degree chevron angle has a higher torque than the 62.5-degree core for all values of pre-strain. This should be investigated further in future studies.

The effects of core and facesheet thickness on the objectives are shown in Figure 8a. It shows an approximately proportional gain in torque for each incremental increase in facesheet thickness. However, an incremental increase in core thickness results in a gain in torque which is greater for a thicker core. This highlights the core's role in increasing the distance between the facesheets and the neutral plane, which increases the out-of-plane stiffness of the panel. The increased out-of-plane stiffness also reduces the curvature metric, as shown in the figure. Note that thicker facesheets also reduce the curvature metric but at a higher cost to torque.

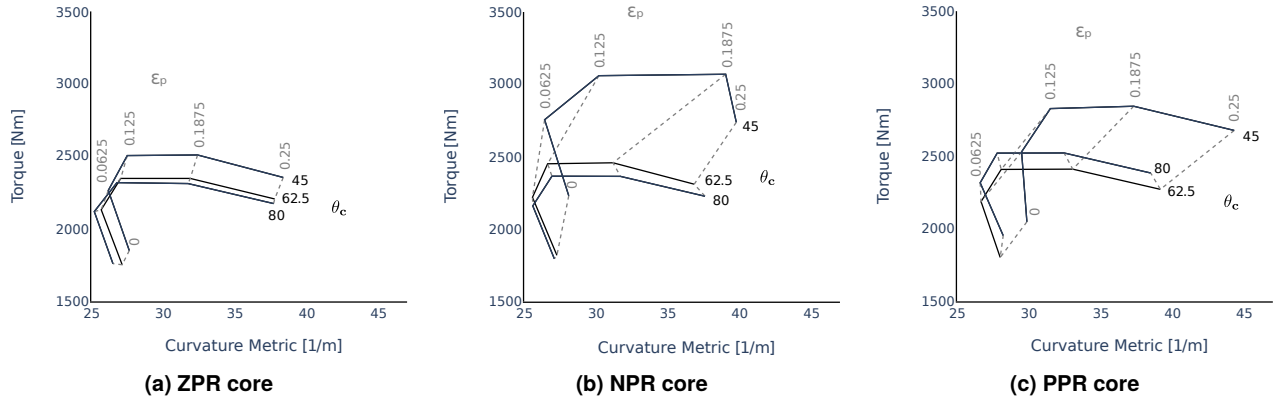


FIGURE 7: PARAMETRIC STUDY OF CHEVRON ANGLE AND APPLIED PRE-STRAIN ON EACH CORE TYPE.

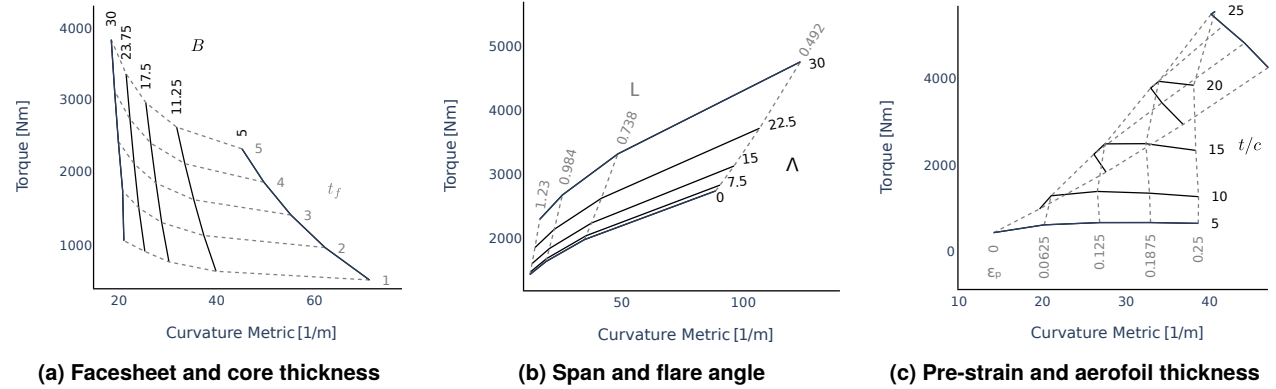


FIGURE 8: PARAMETRIC STUDY OF THE CORRELATED VARIABLES

The effects of span and flare angle on the objectives are shown in Figure 8b. Note that non-zero flare angles break the symmetry of the model. Hence, the full model was used for this study. An increase in flare angle increases both torque and curvature. Both of these are attributed to the increase in the panel length along the hinge. Note that the main contribution to the curvature metric comes from the curvature κ_{11} around the 2-axis. Hence, any increase in the panel length along the 2-axis results in an increased curvature metric. Additionally, the figure shows a reduction in torque and curvature with increasing span. This agrees with the conclusions drawn in the previous analytical research by authors on a simplified wingtip joint fairing model [5].

The effects of pre-strain on the objectives for various thickness-to-chord ratios of the aerofoil are shown in 8c. The torque-curvature response of the fairing significantly changes with the thickness of the aerofoil. For thicker aerofoils with lower pre-strain, an incremental increase in pre-strain increases torque and decreases curvature. However, above a certain pre-strain level, the direction of change in torque and curvature for an incremental increase in pre-strain reverses. This effect is further explored for the 25% thickness-to-chord ratio aerofoil in Figure 9. It shows a lower initial stiffness for the cases with higher pre-strain. These cases show a longer linear region with a later softening on the torque-rotation curve. In contrast, cases with lower pre-strain start with a higher initial stiffness but soften earlier due to the out-of-plane deformation of the panel. The earlier

increase in the out-of-plane deformation of the panel is indicated by the earlier increase in the curvature metric. The difference in the out-of-plane deformation due to pre-strain is further illustrated in Figure 10. The study indicates that pre-strain helps both extend the linear stiffness region of the fairing and reduce the warping of the cross-section shape. However, this improved shape retention comes at the cost of higher torque values at high rotation angles, as the non-linearity being delayed with pre-strain is a softening non-linearity.

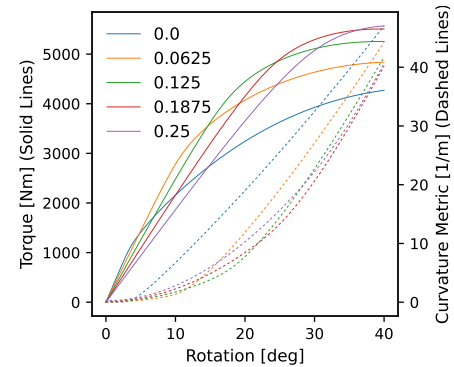


FIGURE 9: TORQUE-CURVATURE PLOT FOR VARIOUS PRE-STRAIN ON A 25% THICKNESS-TO-CHORD RATIO AEROFOIL.

The analysis and the results presented here identify the variables which have significant effects on the objectives, thereby enabling the design space to be reduced without a great compro-

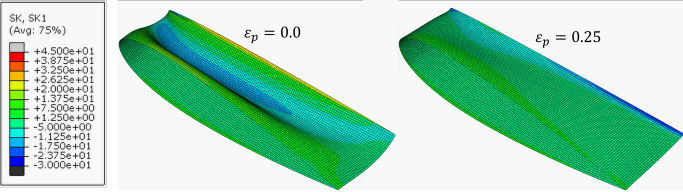


FIGURE 10: DEFORMATION FOR VARIOUS PRE-STRAIN ON A 25% THICKNESS-TO-CHORD RATIO AEROFOIL.

mise on potentially good solutions. The reduced design space allows a more detailed parametric study of the design variables. The parametric study provides further physical insight into the competing objectives of these compliant fairings. It also shows that careful choice of the design variables can lead to very different responses, in both magnitude and shape, in a manner that provides many useful options for designing these GATOR panels for compliant fairings.

4. CONCLUSION

The paper presented a parametric analysis of a morphing fairing around a hinged wingtip joint. The fairing is made of GATOR morphing skin panels on a pivoted-rib support structure. The study identified the variables that are highly correlated with the objectives of reducing torsional stiffness and maintaining a smooth cross-section shape. Higher chevron angles, thinner facesheets and a thicker core are desirable for the GATOR panels. Zero Poisson's ratio core further outperformed the positive and negative Poisson's ratio cores. Longer span and ~~smaller~~larger flare angles gave better results for the wing section. Applied pre-strain of the panel trades off the lower torsional stiffness against a smoother cross-section shape. Moreover, unlike the other variables, the direction of the trends between the pre-strain and the objectives reverses across a threshold pre-strain value. The correlated variables and trends identified in this study help to reduce the design space for further analysis and optimisation.

REFERENCES

- [1] Wilson, Thomas, Kirk, James, Hobday, John and Castrichini, Andrea. "Small scale flying demonstration of semi aeroelastic hinged wing tips." *19th International Forum on Aeroelasticity and Structural Dynamics (IFASD 2019)*. 2019. Savannah, Georgia, USA.
- [2] Castrichini, Andrea. "Parametric Assessment of a Folding Wing-Tip Device for Aircraft Loads Alleviation." Phd thesis, University of Bristol. 2017. URL <https://bris.on.worldcat.org/oclc/1052838653>.
- [3] Siddaramaiah, V. Hodigere, Calderon, D. E., Cooper, J. E. and Wilson, T. "Preliminary Studies in the use of Folding Wing-tips for Loads Alleviation." *Royal Aeronautical Society Applied Aerodynamics Conference*. 2014. Bristol, UK.
- [4] Wilson, T., Azabal, A., Castrichini, A., Cooper, J., Ajaj, R. and Herring, M. "Aeroelastic behaviour of hinged wing tips." *5th Aircraft Structural Design Conference*. 2016. Royal Aeronautical Society, Manchester, United Kingdom. URL <https://eprints.soton.ac.uk/400895>.
- [5] Mahid, Nuhaadh Mohamed and Woods, Benjamin King Sutton. "Initial exploration of a compliance-based morphing fairing concept for hinged aerodynamic surfaces." *Aerospace Science and Technology* (2023): p. 108244 DOI [10.1016/j.ast.2023.108244](https://doi.org/10.1016/j.ast.2023.108244).
- [6] Heeb, Rafael M, Dicker, Michael and Woods, Benjamin K S. "Manufacturing and characterisation of 3D printed thermoplastic morphing skins." *Smart Materials and Structures* Vol. 31 No. 8 (2022): p. 085007. DOI [10.1088/1361-655x/ac71ed](https://doi.org/10.1088/1361-655x/ac71ed).
- [7] Woods, Benjamin KS and Heeb, Rafael M. "Design principles for geometrically anisotropic thermoplastic rubber morphing aircraft skins." *Journal of Intelligent Material Systems and Structures* (2022): p. 1045389X2210961DOI [10.1177/1045389X221096155](https://doi.org/10.1177/1045389X221096155).
- [8] Bubert, Edward A., Woods, Benjamin K. S., Lee, Keejoo, Kothera, Curt S. and Wereley, N. M. "Design and Fabrication of a Passive 1D Morphing Aircraft Skin." *Journal of Intelligent Material Systems and Structures* Vol. 21 No. 17 (2010): pp. 1699–1717. DOI [10.1177/1045389X10378777](https://doi.org/10.1177/1045389X10378777).
- [9] Olympio, Kingnidé Raymond and Gandhi, Farhan. "Zero Poisson's Ratio Cellular Honeycombs for Flex Skins Undergoing One-Dimensional Morphing." *Journal of Intelligent Material Systems and Structures* Vol. 21 No. 17 (2009): pp. 1737–1753. DOI [10.1177/1045389X09355664](https://doi.org/10.1177/1045389X09355664).
- [10] Kothera, Curt S, Woods, Benjamin KS, Wereley, Norman M, Chen, Peter C and Bubert, Edward A. "Cellular support structures used for controlled actuation of fluid contact surfaces." (2011). U.S. Patent No. 7,931,240.
- [11] Olympio, Kingnidé R. and Gandhi, Farhan. "Flexible Skins for Morphing Aircraft Using Cellular Honeycomb Cores." *Journal of Intelligent Material Systems and Structures* Vol. 21 No. 17 (2009): pp. 1719–1735. DOI [10.1177/1045389X09350331](https://doi.org/10.1177/1045389X09350331).
- [12] Dassault Systems. "Shell section behavior: Transverse shear stiffness." *Abaqus Documentation: Abaqus Elements Guide*. Dassault Systems (2018).
- [13] Pagano, N.J. "Exact Solutions for Rectangular Bidirectional Composites and Sandwich Plates." *Journal of Composite Materials* Vol. 4 No. 1 (1970): pp. 20–34. DOI [10.1177/002199837000400102](https://doi.org/10.1177/002199837000400102).
- [14] Whitney, James Martin. *Structural analysis of laminated anisotropic plates*. Technomic Pub. Co. (1987).
- [15] Dassault Systems. "Transverse shear stiffness in composite shells and offsets from the midsurface." *Abaqus Documentation: Abaqus Theory Guide*. Dassault Systems (2018).
- [16] Geuzaine, Christophe and Remacle, Jean-François. "Gmsh: A 3-D finite element mesh generator with built-in pre- and post-processing facilities." *International Journal for Numerical Methods in Engineering* Vol. 79 No. 11 (2009): pp. 1309–1331. DOI [10.1002/nme.2579](https://doi.org/10.1002/nme.2579).